Inertia Emulation and Fast Frequency-Droop Control Strategy of a Point-to-Point VSC-HVdc Transmission System for Asynchronous Grid Interconnection

Jiebei Zhu, *Senior Member, IEEE*, Xiaonan Wang, Junbo Zhao, *Senior Member, IEEE*, Lujie Yu, Suxuan Li, Yunwei Li, *Fellow, IEEE*, Josep M. Guerrero, *Fellow, IEEE*, and Chengshan Wang, *Senior Member, IEEE*

***Abstract*—This article proposes a novel inertia emulation and fast frequency-droop (IEFF) control strategy for a point-to-point voltage source converter-based high voltage direct current (VSC-HVdc) transmission system. It allows asynchronous ac grid synchronization in forms of inertial and fast frequency-droop responses provided to "both" sides of the VSC-HVdc interconnected grids, different from the historically reported schemes only providing these responses to one grid. Under the IEFF scheme, the power-regulating VSC (PR-VSC) station emulates a synchronous generator directly through its active power control, whereas the dc-voltage-regulating VSC (DR-VSC) station employs a dc voltage/frequency droop control to convey its connected grid frequency communication-free to the remote PR-VSC for inertial and fast frequency-droop oriented power variations. To avoid the clash of the PR-VSC IEFF and DR-VSC IEFF control under simultaneous frequency events in the asynchronous grids, a novel frequency support mode selection scheme is designed to effectively prioritize the IEFF support with a higher frequency gradient. The key parameters of the IEFF controller are optimized through small signal stability analysis. The effectiveness of the proposed IEFF scheme is verified through controller hardware-in-the-loop experiments. The results show that the proposed IEFF scheme effectively promotes synchronization and enhances overall frequency stability for the two interconnected asynchronous grids.**

***Index Terms*—Frequency response, high voltage direct current (HVdc) transmission, power control, power system stability.**

Manuscript received May 26, 2021; revised July 14, 2021, October 15, 2021, and December 21, 2021; accepted December 28, 2021. Date of publication January 4, 2022; date of current version February 18, 2022. This work was supported in part by the National Key Research and Development Program of China under Grant 2018YFA0702200 and in part by the National Natural Science Foundation of China under Grant 51977143. Recommended for publication by Associate Editor B. Singh. *(Corresponding authors: Lujie Yu; Suxuan Li.)*

Jiebei Zhu, Xiaonan Wang, Lujie Yu, Suxuan Li, and Chengshan Wang are with the School of Electrical and Information Engineering, Tianjin University, Tianjin 300072, China (e-mail: jiebei.zhu@tju.edu.cn; 18713596838@163.com; lujie.yu@outlook.com; xx970515@163.com; cswang@tju.edu.cn).

Junbo Zhao is with the Department of Electrical and Computer Engineering, University of Connecticut, Storrs, CT 06269 USA (e-mail: junbo@uconn.edu).

Yunwei Li is with the Department of Electrical and Computer Engineering, University of Alberta, Edmonton, AB T6G 1H9, Canada (e-mail: yunwei.li@ualberta.ca).

Josep M. Guerrero is with the Department of Energy Technology, Aalborg University, 9220 Aalborg, Denmark (e-mail: joz@et.aau.dk).

Color versions of one or more figures in this article are available at https://doi.org/10.1109/TPEL.2021.3139960.

Digital Object Identifier 10.1109/TPEL.2021.3139960

NOMENCLATURE

H, H_A, H_B	Inertia time constants of a SG, the PR-VSC, and the DR-VSC (in second).
D, D_A, D_B	Droop coefficients of a SG, the PR-VSC, and the DR-VSC (in p.u.).
f, f_A, f_B	Instantaneous frequencies of a SG, the Grid A, and the Grid B (in p.u.).
f_0, f_{A0}, f_{B0}	Nominal frequencies of a SG, the Grid A, and the Grid B (in p.u.).
f_{VB}	Estimated Grid B frequency (in p.u.).
P_M, P_E, T_m, T_e	Mechanical and electrical power and torque of SG (in p.u.).
P_A^*, P_A, P_{A0}^*	Active power reference, active power, and active power reference value of the traditional control of the PR-VSC outer controller (in p.u.).
Q_A, Q_B, Q_A^*, Q_B^*	Reactive power and reactive power reference of PR-VSC and DR-VSC (in p.u.).
V_{dcA}, V_{dcB}, V_{dcB}^*, V_{dcB0}	DC voltages at the dc terminals of PR-VSC and DR-VSC, dc voltage reference and nominal value of DR-VSC (in p.u.).
k_{dc}	Coefficient of V_{dc} / f droop control.
R_{dc}, L_{dc}, C	Equivalent dc resistance, inductance, and parallel capacitor (in p.u.).
I_{dc}, i_{dcA}, i_{dcB}	DC current, PR-VSC, and DR-VSC dc currents (in p.u.).
p	Differential operator.
f_{DL}, f_{DH}	Lower and upper-triggering frequency thresholds of the dead zone (in Hz).
x, u, A, B	State vector, input vector, state transition matrix, and input matrix.
i_{sgA}, i_{sgB}, v_{sgA}, v_{sgB}	Terminal currents and voltages of SG A and B (in p.u.).
i_{t1}, i_{t2}	Transformer currents of Girds A and B (in p.u.).

v_r, v_s, i_s	Voltages and current of the impedance on the ac outlet side of VSCs (in p.u.).
$R_L + jX_L$, $R_S + jX_S$	Impedance of the ac loads and transmission lines.
θ_1, θ_2, θ_{sg}	Phase angles of PR-VSC, DR-VSC, and SG.
k_{pp}, k_{pq12}, k_{pdc}, k_{ip}, k_{iq12}, k_{idc}, k_{pi}, k_{ii}	Proportional and integral gains of the PR-VSC and DR-VSC outer controller and inner control.
i^*_{dq}, i_{dq}	dq-axis current references from outer controllers and converter currents (in p.u.).
v^*_{dq}, v_{abc}	dq-axis and abc-axis voltage references from inner current controller (in p.u.).
P_{PR-VSC}, P_{DR-VSC}	Active power outputs of PR-VSC and DR-VSC (in p.u.).
ω_r, ω_{pll}, ω_{sgAr}, ω_{sgBr}	Angular velocities of a SG rotor, the PLL of VSCs, the SG A, and SG B rotor (in p.u.).
$\boldsymbol{V}_{sg6\times1}$, $\boldsymbol{R}_{6\times6}$, $\boldsymbol{I}_{sg6\times1}$, $\boldsymbol{\varphi}_{sg6\times1}$	SG voltage, resistance, current, and flux linkage vectors in dq-axis.
T_r, K_{fd}, T_{fd}	Time constant of the low-pass filter, the gain and time constant of the damping filter of the SG excitation system.
K_a, T_a, v_{f0}	Gain, time constant of the excitation system regulator, and the initial value of the excitation voltage.
K_p, R_p	Proportional coefficient and droop coefficient of the steam turbine regulator.
T_{sr}, T_{sm}	Time constants of the steam turbine speed relay and the servo motor.
$T_1 - T_4$, $F_2 - F_5$	Time constants and torque friction coefficients of the steam turbine.
$z_{1i} - z_{6i}$	Integral terms of the PID controllers.
R_t, R_{rc}, R_c, L_t, C_{rc}, L_c	Equivalent resistances, capacitances, and inductances of transformer, series *RC* load and ac line of converter (in p.u.).
v_{cd}, v_{cq}, i_{cd}, i_{cq}	dq-axis capacitor voltage and current of the series *RC* load (in p.u.).

I. Introduction

In THE past decade, the share of renewables in the total energy sources has experienced significant prosperity all over the world. By the end of 2019, the renewable energy sources (RES) in the world account for 41% of the total primary energy, exceeding the share of nuclear power for the first time [1]. To ensure the power balance between RES and demand, high extents of asynchronous grid interconnections are necessary. For example, in Europe, dc interconnections are desired to facilitate electricity trading among disperse national grids and deliver offshore wind power generated in Nordic Seas to adjacent countries [2]. In Asia, grid interconnections are also increasingly demanded [3], [4].

Voltage source converter-based high voltage direct current (VSC-HVdc) transmission systems have been regarded as a preferred technology in recent years due to its advantages of flexible control capability, the ease of power reversal, and the mitigation of commutation failure [5], [6], as compared with the traditional HVdc technology. In general, for a point-to-point VSC-HVdc system control, one converter station acts as a power-regulating VSC (PR-VSC), while the other one must act as a dc-voltage-regulating VSC (DR-VSC). However, under such a traditional control (TC) scheme, the converters are unable to participate in transient stability regulation for any of the two interconnected grids [7]. In fact, the traditional control scheme decouples the interconnected asynchronous grids in transient states and denies the possible mutual support when one side grid experiences a significant frequency event.

To implement synchronization mechanism for the VSC-HVdc system, advanced control methods have been developed to enable power synchronization or mimic synchronous generation (SG) behaviors for VSC-connected grids [8]–[13]. However, the energy sources to achieve such effects are not detailed in these works, and the claimed effects can only be provided to one grid by a designated VSC station. Other control schemes proposed in [7] and [14]–[17] consider the dc capacitor as its energy source for inertia provision and utilize the power from one grid for frequency-droop emulation to support the other grid. However, the energy stored in typical VSC-HVdc capacitors is limited and the capacitors must be uneconomically augmented to realize the desired inertial response. Moreover, such schemes can only support one grid by the inertia and frequency-droop control.

To achieve the mutual support of VSC-HVdc interconnected power grids, references [18], [19] develop a master–slave control scheme, where the two VSCs can exchange the frequency information of their respectively connected grids to the other side through communications. In [20], the frequency consensus algorithm with communication is used to modify converter power reference, ensuring the desired frequency support between the separate ac grids. Similarly, Veganzones *et al.* [21] realize flexible frequency support between multiterminal HVdc interconnected systems. But the active power of each converter must be locally measured and centrally collected in the master control via communication channels under the frequency support schemes. The drawback is that communications may introduce control delay, compromise control reliability, and increase capital costs. Gao *et al.* [22]–[24] propose several droop-based power sharing control strategies without the need of communication, but they only consider the accuracy of the power sharing for multiple converters and do not involve any frequency support functionality. In [25]–[28], communication-free approaches with inertia and primary frequency support from offshore wind farms integrated HVdc systems to onshore ac grid are proposed without exploring the possibility of the reversed support from the onshore grid to offshore grid. In [29] and [30], a virtual friction control scheme is proposed by introducing coupled inertial and frequency-droop dynamics between two asynchronous grids, but this frequency support can only be provided for one designated grid. Some valuable work has been conducted to emulate the inertial and

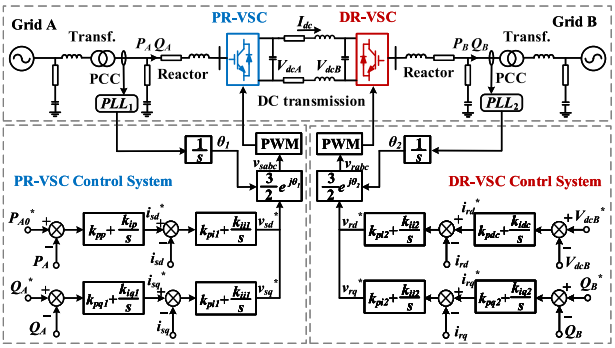

Fig. 1. Single-line diagram of VSC-HVdc transmission system with the traditional control.

frequency-droop effects through the grid forming converters. However, the grid forming converters as presented in [8]–[10] do not include inner current control loop, which may cause issues during fault current limiting. The grid forming converter control scheme as presented in [13], although consisting of inner current control and voltage control loop, inevitably increases the control complexity. On the other hand, the converters with the traditional current control are already widely in commission all over the world. It is much easier for the manufacturers to realize the inertia and frequency-droop emulation based on the modification of the mature control scheme.

This article proposes a new inertia emulation and fast frequency-droop (IEFF) strategy for VSC-HVdc transmission system, which can securely provide mutual frequency support for "both" sides of the interconnected asynchronous grids. In particular, there is no control scheme yet which enables DR-VSC to provide inertia and frequency-droop responses in the existing literature, as it is difficult for DR-VSC to directly dictate the active power control. The proposed IEFF scheme right resolves such a difficulty. The main features of the IEFF are the following.

1) The inertial and frequency-droop responses can be "autonomously" provided to both grids.
2) A dc voltage/frequency control loop is ingeniously embedded in the DR-VSC local control to convey its instantaneous grid frequency to the PR-VSC station, accommodating active power variations for designated inertial and frequency-droop responses.
3) A priority selection control loop is proposed to decide the priority of supported grid under simultaneous frequency events in the two asynchronous grids with a specified minimum service duration.

The rest of this article is organized as follows. The proposed IEFF scheme is detailed in Section II. Section III presents control parameter optimization based on small-signal analysis (SSA). In Section IV, controller hardware-in-the-loop (C-HIL) experiments are conducted to verify the effectiveness of the proposed control. Finally, Section V concludes this article.

II. Proposed IEFF Scheme for VSC-HVdc Interconnected Asynchronous Grids

A candidate VSC-HVdc interconnected asynchronous grid is illustrated in Fig. 1. The traditional VSC-HVdc outer loop and

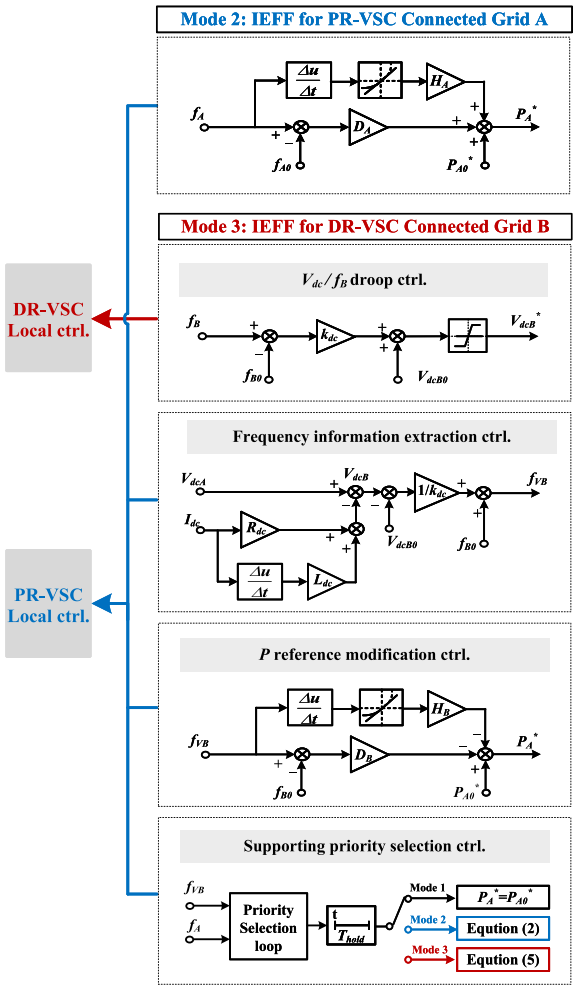

Fig. 2. Proposed IEFF scheme for VSC-HVDC.

inner current loop can be found in [14], and thus, not repeated in detail here. This section will present the core design process of the proposed IEFF, including the PR-VSC IEFF and the DR-VSC IEFF.

A. IEFF for PR-VSC Connected Grid

The active power controller of the PR-VSC is directly modified to emulate SG dynamic characteristics by embedding the following well-known SG swing equation:

$$2H \cdot \frac{df}{dt} = P_M - P_E - D\,(f - f_0) \tag{1}$$

where H is the emulated inertia time constant, and D is the fast-frequency-droop control coefficient.

The PR-VSC control loop, as illustrated in Fig. 2 (titled as "Mode 2," the TC mode is defined as "Mode 1"), is designed to change the active power reference of PR-VSC to mimic the SG inertial and frequency-droop behaviors for Grid A via

$$P_A^* = P_{A0}^* - D_A\,(f_A - f_{A0}) - 2H_A \cdot \frac{df_A}{dt}. \tag{2}$$

The rate of change of frequency (RoCoF) df_A/dt is computed by a discrete first-order time-derivative module as shown in the top of Fig. 2. To estimate the instantaneous RoCoF, conventional

RoCoF relay for islanding protection application has a large measurement window of around 500 ms, mainly to avoid the maloperation of the RoCoF relay and avoid control noise in a short time window. However, with a large measurement window, the disadvantage is that the sensitivity of nondetection zones can be reduced and the estimation accuracy may be compromised. Therefore, a moderate RoCoF measurement window of 10 ms is recommended and adopted in this article.

B. IEFF for DR-VSC Connected Grid

As the control objective of the DR-VSC station is to maintain the power balance in the HVdc system by regulating the dc link voltage, it passively delivers the transmitted active power of PR-VSC via the dc link and as a result exerts no direct control of the power flow to its connected Grid B. To accommodate the required power variation for the proposed IEFF to the DR-VSC connected Grid B, the remote PR-VSC station must be coordinated in its local control. Moreover, as discussed before, communication for the coordination of the IEFF should be avoided in the IEFF scheme.

The proposed DR-VSC IEFF control conveys the frequency of the DR-VSC connected grid to the PR-VSC control for the power variation. Different from [18] and [19], this approach favorably takes advantage of physical electrical characteristics that are already known or always measurable on the PR-VSC side. Four essential control loops of the proposed IEFF scheme for the DR-VSC connected grid are summarized as follows.

1) In the DR-VSC control, a V_{dc}/f droop control loop for the Grid B frequency and the dc terminal voltage of DR-VSC is proposed. This allows a quantified correlation of the Grid B frequency variation with the dc voltage variation.
2) In the PR-VSC control, an information extraction control loop is designed to restore the instantaneous frequency information of the remote Grid B based on the dc voltage variation measured at the PR-VSC terminal.
3) In the PR-VSC control, its active power reference modification loop is used to execute the required power variation for achieving different supporting modes.
4) In the PR-VSC control, a priority selection control loop is proposed to determine which grid, i.e., Grid A or Grid B as shown in Fig. 1, is supported first by the IEFF, according to the comparisons of their respective frequency gradients.

1) VDC / f Droop Control Loop in the DR-VSC Control: To reflect the Grid B frequency on the DR-VSC terminal dc voltage, a dc voltage/frequency droop control loop as shown in Fig. 2 is implemented in the DR-VSC control via

$$V_{dcB}^{*} = k_{dc}(f_B - f_{B0}) + V_{dcB0}. \tag{3}$$

The droop control loop correlates the dc voltage variation of $\pm 10\%$ of the nominal value, which will not significantly affect the system operation stability [14], with the Grid B frequency variations of ± 2 Hz. The optimization of the droop coefficient k_{dc} will be discussed in the next section.

2) Frequency Information Extraction Control Loop: To enable the IEFF support to Grid B, the active power of PR-VSC station must vary correspondingly with the remote Grid B frequency. As designed in Section II-B-1, the Grid B instantaneous frequency information is included in the dc voltage variation dictated by the V_{dc}/f droop control loop of (3). To extract the Grid B frequency in the PR-VSC local control, an information extraction control loop without communication is designed here, considering the effect of the dc network parameters.

As the dc terminal voltages of PR-VSC and DR-VSC are different due to the existence of dc resistance and reactance, the dc voltage measured at the PR-VSC terminal must take account of the dc line voltage drop. Although distributed frequency dependent cable modeling approach retains the most fidelity of a dc transmission line, its relative complex structure and mathematical expressions reduces the necessity when the line drop compensation is the main focus. Instead, the total equivalent resistance and reactance of the dc network are lumped here as they are the most influential factors. The overall accuracy of such a simplification is validated later in the experimental results. Thus, the Grid B frequency information can be extracted by considering (3) as well as the total dc network impedance as shown in Fig. 2

$$\begin{cases} V_{dcA} = V_{dcB} + R_{dc}I_{dc} + L_{dc}\dfrac{dI_{dc}}{dt} \\ \Delta V_{dcB} = V_{dcA} - R_{dc}I_{dc} - V_{dcB0} - L_{dc}\dfrac{dI_{dc}}{dt} \\ f_{VB} = f_{B0} + \dfrac{\Delta V_{dcB}}{k_{dc}}. \end{cases} \tag{4}$$

R_{dc} and L_{dc} can be obtained from the manufacturing data of VSC-HVdc cable (i.e., resistance density and reactance density times the total cable length). Considering the potential impact of the dc impedance variations on the performance of the frequency information extraction, R_{dc} and L_{dc} values employed in (4) should be periodically calibrated using cable measurement techniques (e.g., traveling wave propagation measurement as in [31]). Having said that though, with the variations of the dc circuit R_{dc} and L_{dc} as much as $\pm 20\%$ regarding to the values used in the IEFF control, the C-HIL experiment evaluations in Section IV will show that the impedance variations do not affect the IEFF control stability despite of trivial control inaccuracy.

3) Active Power Reference Modification Control Loop: To mimic the SG droop and inertia characteristics as presented in (1), a control loop for the PR-VSC active power reference modification is designed to realize the IEFF for Grid B by using the Grid B frequency information as extracted in (4), yielding

$$\begin{aligned} P_A^{*} &= P_{A0}^{*} - D_B(f_{VB} - f_{B0}) - 2H_B\frac{df_{VB}}{dt} \\ &= P_{A0}^{*} - \frac{D_B\Delta V_{dcB} + 2H_B\left(\dfrac{dV_{dcA}}{dt} - R_{dc}\dfrac{dI_{dc}}{dt} - L_{dc}\dfrac{d^2I_{dc}}{dt^2}\right)}{k_{dc}} \\ &= P_{A0}^{*} - K_1\Delta V_{dcB} - K_2 pV_{dcA} + K_3 pI_{dc} + K_4 p^2 I_{dc} \end{aligned} \tag{5}$$

where $K_1 = D_B/k_{dc}$; $K_2 = 2H_B/k_{dc}$; $K_3 = 2H_B R_{dc}/k_{dc}$; and $K_4 = 2H_B L_{dc}/k_{dc}$.

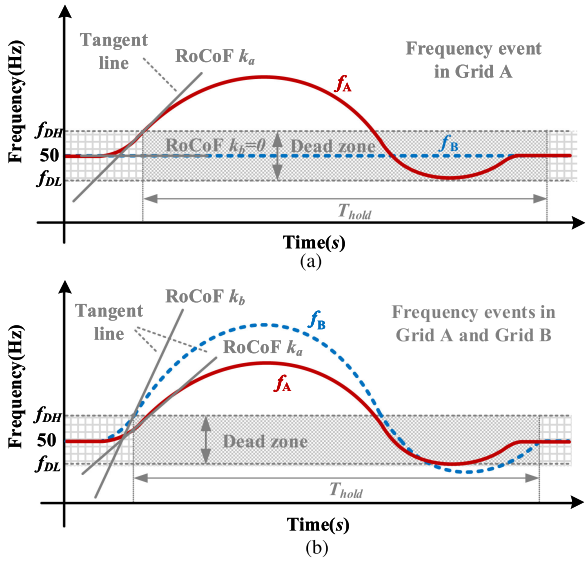

Fig. 3. Comparison of RoCoFs. (a) Frequency event occurs in Grid A. (b) Simultaneous frequency events occur in Grid A and Grid B.

It can be indicated that by correlating dc voltage with Grid B frequency as (3), the PR-VSC can estimate the instantaneous Grid B frequency by (4) and adjust its active power by (5), so as to provide the IEFF for Grid B.

PR-VSC active power reference is then calculated fitting into one of three complementary operating modes: 1) Mode 1—traditional active power control; 2) Mode 2—IEFF support for the local Grid A as designed in (2); 3) Mode 3—IEFF support for the remote Grid B as designed in (3) and (5). The corresponding PR-VSC active power reference is thus expressed as

$$P_A^* = \begin{cases} P_{A0}^*, \text{Mode1} \\ \text{Eq.}(2), \text{Mode2} \\ \text{Eq.}(3)-(5), \text{Mode3}. \end{cases} \tag{6}$$

4) Priority Selection Control Loop in the PR-VSC Control: As discussed earlier, simultaneous frequency events may occur in Grid A and Grid B, which cannot be addressed by the IEFF at the same time. Thus, the IEFF support priority must be decided to avoid further disturbance caused by the VSC-HVdc transmitted active power flow. In other words, when the IEFF support for one grid is activated, the support for the other grid must be deactivated. A priority selection control loop is designed in the PR-VSC control to compare the RoCoFs of Grid A and Grid B in the PR-VSC control, which will activate the IEFF support to the grid with higher RoCoF and deactivate the other one for a minimum service duration.

The comparisons of RoCoF under different typical events are displayed in Fig. 3. In particular, for Fig. 3(a), if a frequency event occurs in Grid A, the priority selection control loop compares the Grid A frequency and Grid B frequency at the time point immediately when Grid A frequency overruns the dead zone, and activates the IEFF support to Grid A with higher RoCoF and deactivates the IEFF for Grid B. By contrast, for Fig. 3(b), if simultaneous frequency events occur in Grid A and Grid B, the priority selection unit compares both RoCoFs immediately when one grid frequency overruns the dead zone, and prioritizes support to one grid (in this case it is Grid B).

Algorithm 1: Mode Selection.

Input: f_A, f_B, df_A/dt, df_B/dt
Output: $Mode$ // $Mode$ is a determined mode
if N=0 **then** // N is the number of calculation steps
if $f_{DL} \le f_A \le f_{DH}$ & $f_{DL} \le f_B \le f_{DH}$ **then**
M=1
N=1
end if
if $f_A < f_{DH}$ || $f_A > f_{DH}$ || $f_B < f_{DH}$ || $f_B > f_{DL}$ **then**
if $|df_A/dt| \ge |df_B/dt|$ **then**
M=2
end if
if $|df_A/dt| < |df_B/dt|$ **then**
M=3
end if
N=$T_{hold} \times h$ // h is the number of calculation steps per second
end if
N=N-1
return $Mode$

A dead zone is configured in this priority selection control loop by a lower boundary f_{DL} and a higher boundary f_{DH}, as shown in Fig. 3, to avoid unnecessary execution of the IEFF under negligible frequency variations. The threshold setting shall refer to specific system operation requirements. For instance, the U.K. operation codes require the system must operate with the frequency between [49.9, 50.1 Hz] in steady states [32]. Thus, the thresholds of [f_{DL} = 49.9 Hz, f_{DH} = 50.1 Hz] are adopted in this article. A minimum service duration T_{hold} is applied for the mode selection loop to hold an activated mode for a fixed period, so as to avoid possible frequent mode switching actions causing unnecessary power disturbances to the two asynchronous grids. The comparisons of Grid A and Grid B frequency are executed with a fixed time interval of the minimum service duration T_{hold}. T_{hold} in this article is set as 10 s.

The PR-VSC active power reference should lie in one of the three operating modes according to the decision of the priority selection control loop. The selection principles of the three modes are expressed as follows:

$$\text{Mode} = \begin{cases} \text{Mode 1, when } f_A \wedge f_{VB} \in [f_{DL}, f_{DH}] \\ \text{Mode 2, when} f_A \vee f_{VB} \notin [f_{DL}, f_{DH}] \&\& \left|\frac{df_A}{dt}\right| \ge \left|\frac{df_{VB}}{dt}\right| \\ \text{Mode 3, when} f_A \vee f_{VB} \notin [f_{DL}, f_{DH}] \&\& \left|\frac{df_A}{dt}\right| < \left|\frac{df_{VB}}{dt}\right|. \end{cases} \tag{7}$$

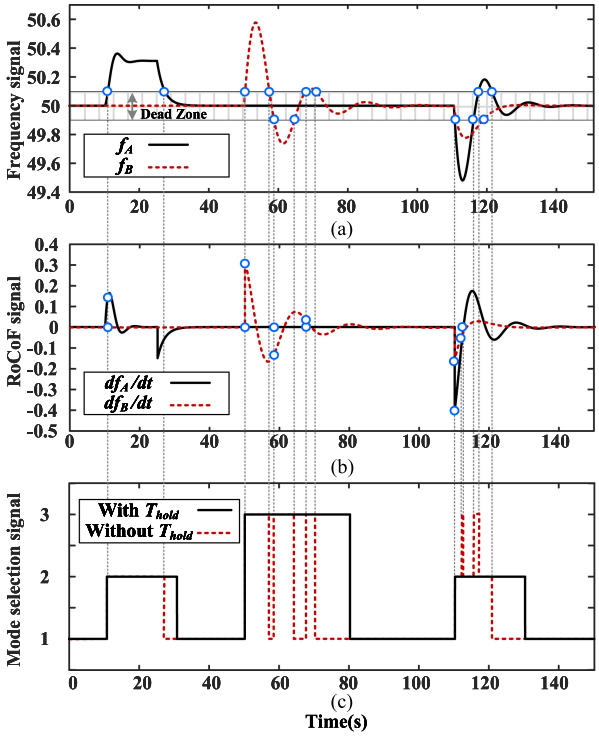

Fig. 4. Verification of frequency selection mode. (a) Analog frequency signal. (b) Analog RoCoF signal. (c) Mode selection signal.

A simulation verification is carried out in MATLAB/Simulink environment to demonstrate the mode selection process as well as the necessity of the minimum service duration, under different Grid A and Grid B frequency events. The times when the frequencies exceed and withdraw to the dead zone and the comparisons of the instantaneous RoCoFs are highlighted with blue circles in Fig. 4.

The pseudocode of (7) is presented as follows.

It can be observed from Fig. 4(a) that the input Grid A frequency f_A experiences a step change of 0.3 Hz at $t = 10$ s and then restores to the nominal value at $t = 30$ s, while the input Grid B frequency f_B remains unchanged at 50 Hz during this period. As can be seen, f_A exceeds f_{DH} and has a higher RoCoF when comparing to that of f_B, as presented in Fig. 4(b). As observed in mode selection decision chart of Fig. 4(c), the solid black line indicates the Mode 2 is selected at $t = 10$ s and deactivated at $t = 30$ s with $T_{hold} = 10$ s. By contrast, the dashed red line shows the selection decision that Mode 2 is triggered at $t = 10$ s and deactivated at $t = 25$ s without T_{hold}.

Another event is also presented in Fig. 4, when the Grid B frequency overruns dead zone at $t = 50$ s, with a RoCoF higher than that of Grid A. With T_{hold}, Mode 3 is selected and sustained for 50 s until $t = 80$ s, as observed in Fig. 4(c). By contrast, without T_{hold}, Mode 3 is unfavorably triggered ON and OFF frequently, causing disturbances to the overall system.

Another simultaneous frequency variation in both Grid A and Grid are applied from $t = 110$ s to $t = 150$ s, with a higher Grid A frequency deviation and RoCoF than those of Grid B. It can be seen from Fig. 4(c), with selected T_{hold}, the supporting priority is correctly fixed at Mode 2, and the undesired reciprocating switching between Mode 2 and Mode 3 are effectively avoided.

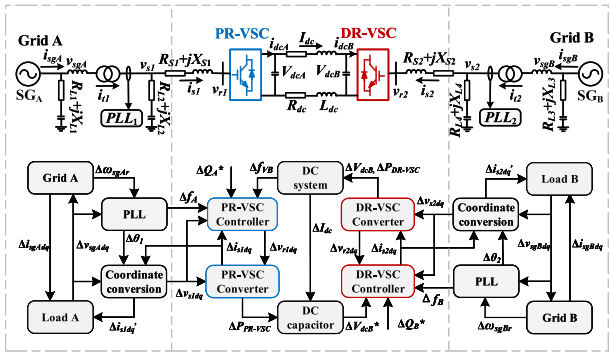

Fig. 5. Two-area asynchronous grid system and corresponding SSM interface diagram.

III. Small Signal Analysis for IEFF Controllers

To optimize the parameters of the proposed IEFF control, a VSC-HVdc interconnected two-area system which consists of two generators (each is located in one area as shown in the top of Fig. 5) is studied, with VSC-HVdc, SG, and control parameters presented in Tables I–III of Appendix B.

The small-signal model (SSM) is established based on the state-space modular subsystems of the grid and control systems as seen in the bottom of Fig. 5, with matrix equations presented in Appendixes A and B. The state-space model of the entire system is described as

$$\dot{\mathbf{x}} = \mathbf{A}\mathbf{x} + \mathbf{B}\mathbf{u}. \tag{8}$$

After linearization, the SSM is expressed as

$$\Delta\dot{\mathbf{x}} = \frac{\partial \mathbf{A}}{\partial \mathbf{x}}\Delta\mathbf{x} + \frac{\partial \mathbf{B}}{\partial \mathbf{x}}\Delta\mathbf{u}. \tag{9}$$

After obtaining the SSM, its accuracy validation is carried out by comparing with its time-domain electromagnetic transient (EMT) model simulated in MATLAB/Simulink platform. As shown in Fig. 6, a step change of PR-VSC active power reference from 0.466 to 0.471 p.u. and another step change of DR-VSC dc voltage reference from 1 p.u. to 1.005 p.u. are applied at $t = 1$ s and 3 s, respectively. As observed in Fig. 6, the responses of the SSM are aligned with those from the EMT model, demonstrating the accuracy of the SSM. The eigenvalues of the entire system are listed in Table IV of Appendix B, which can be regarded as the visualization basics for assessing stability and optimizing control parameters. The system modes λ_{51} & λ_{52} and λ_{55} & λ_{56} with low bandwidth and poor damping are identified as the dominant modes to be focused.

When conducting the stability analysis for the two asynchronous grids, supporting mode of Mode 2 or Mode 3 is assumed to be activated. The optimal control parameters for the entire VSC-HVdc control systems are identified by the SSA and adopted in the C-HIL experiments in next section. Due to the space constraint, only two important optimizations are presented: the IEFF V_{dc}/f droop control gain and IEFF emulated $H\&D$.

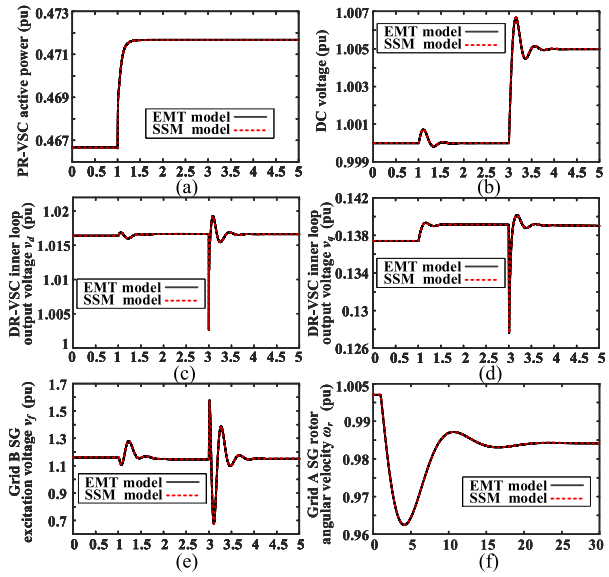

Fig. 6. Step response comparisons between EMT model and SSM model. (a) 0.005 p.u. step active power increasing for PR-VSC. (b) 0.005 p.u. step dc voltage increasing for DR-VSC. (c) DR-VSC inner loop output voltage v_d. (d) DR-VSC inner loop output voltage v_q. (e) Grid B SG excitation voltage. (f) Grid A SG rotor angular velocity.

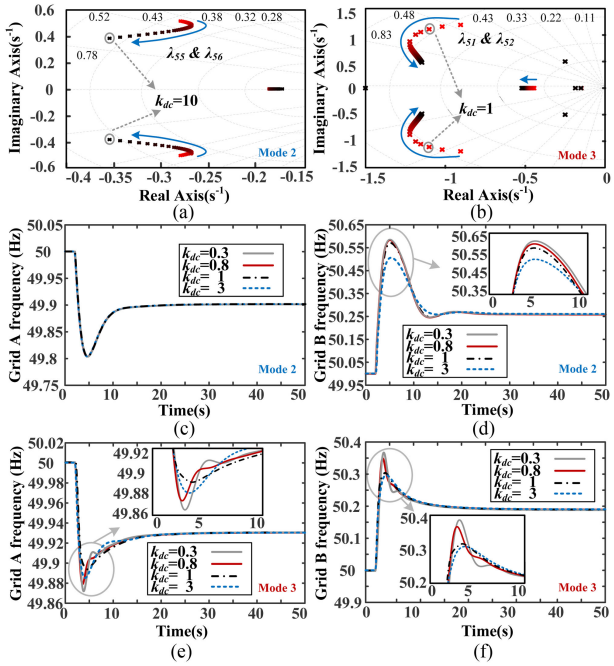

Fig. 7. Root locus and frequency changes in different modes with droop coefficient k_{dc} vary. (a) k_{dc} varies from 0 to 10. (b) k_{dc} varies from 0 to 10. (c) Grid A frequency. (d) Grid B frequency. (e) Grid A frequency. (f) Grid B frequency.

A. Optimization for V_{dc}/f Droop Control Gain

Fig. 7 presents the root locus and frequency changes in different modes when the droop coefficient k_{dc} varies. Initially, all the dominant eigenvalue pair λ lies in the left plane of the root locus chart, indicating the stability of the system. When k_{dc} increases from 0 to 10, as seen in Fig. 7(a), the damping ratio of

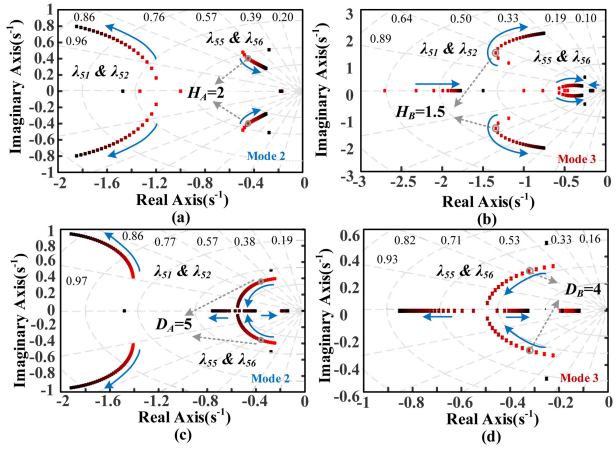

Fig. 8. Root locus where H and D are the virtual inertia time constant and droop coefficient for the IEFF Mode 2 and Mode 3. (a) H_A varies from 0 to 10 s. (d) H_B varies from 0 to 10 s. (e) D_A varies from 0 to 20. (f) D_B varies from 0 to 20.

λ_{55} & λ_{56} is gradually increased, implying the improved system stability. As can be clearly seen in Fig. 7(b), increasing k_{dc} will significantly enhance the damping of λ_{51} & λ_{52}. It can also be observed from Fig. 7(a) and (b) that the influence of the droop coefficient k_{dc} on λ_{51} & λ_{52} is much larger than on λ_{55} & λ_{56}. Thus, the droop coefficient k_{dc} is optimized as 1 with a damping ratio at 0.707 for λ_{51} & λ_{52}.

To test the system performance under different k_{dc}, the PR-VSC active power reference is increased by 0.05 p.u. at $t = 2$ s. Fig. 7(c) and (d) shows that under Mode 2 Grid A frequency stability is not affected but Grid B frequency stability is significantly improved with the optimal k_{dc} at 3 compared to the other three cases. Fig. 7(e) and (f) shows the Grid A and Grid B frequency dynamics under Mode 3. It can be observed that the optimal $k_{dc} = 1$ as identified in Fig. 7(b) results in the lowest overshoot of the Grid A frequency, while having trivial impact on Grid B frequency. This phenomenon is aligned with the conclusion of the root locus analysis.

B. Stability Impact of IEFF Emulated Inertia and Droop

The root locus with emulated inertia time constant H from 0 to 10 s is presented in Fig. 8(a) and (b). Under Modes 2 and 3, the dominant pole pair λ_{55} & λ_{56} approaches the imaginary axis, and the damping ratio is also reduced correspondingly, demonstrating unfavorable stability of the interconnected power grid. However, the subdominant pole pair λ_{51} & λ_{52} in Mode 2 has the opposite movement directions to the imaginary axis, indicating an improved stability for these subdominant modes. Therefore, a reasonable H considering this tradeoff between the dominant mode and subdominant mode is 2 s and 1.5 s, identified for Mode 2 and Mode 3, respectively.

The root locus analysis with emulated droop coefficient D varying from 0 to 20 is carried out under Mode 2 and Mode 3, as seen in Fig. 8(c) and (d), respectively. The results show that the complex conjugate eigenvalues move to more stable areas with enhanced damping ratios. In particular, under Mode 2, with

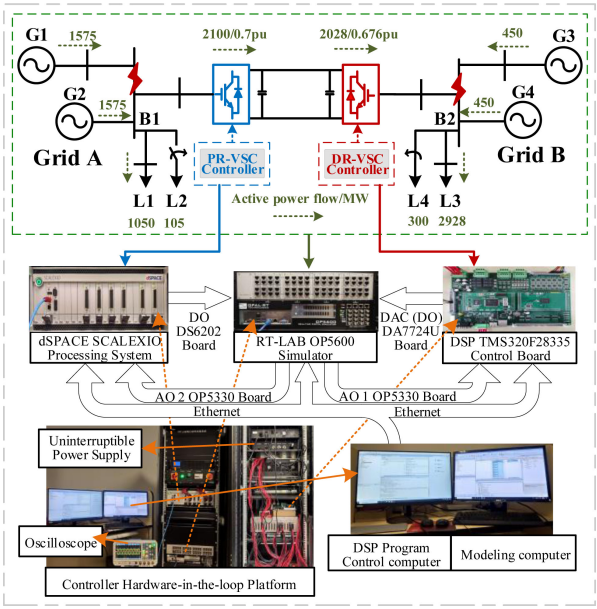

Fig. 9. Test system and experimental C-HIL platform.

the increase of D, the pole pair λ_{51} & λ_{52} moves to a position away from the imaginary axis, implying the enhanced system stability. Thus, D is optimized as 5 and 4 for Mode 2 and Mode 3, respectively.

IV. Experimental Results

A C-HIL experimental platform as shown in Fig. 9 is established to test the effectiveness of the proposed IEFF scheme. As illustrated in Fig. 9, the platform consists of a dSPACE unit prototyping for the PR-VSC IEFF controller, an external DSP-based programmable controller of TMS320F28335 prototyping the DR-VSC IEFF controller, an RT-LAB OP5600 modeling the rest of the modified two-area system [33] and the VSC-HVdc transmission circuits using HYPERSIM toolbox in MATLAB/Simulink. The IEFF performance is evaluated in this article using a three-level VSC converter technology, but it can be equally used in the modular multilevel converter-based HVdc system. The PR-VSC control measures the three-phase voltage output from the system model in RT-LAB, estimates the instantaneous frequency by its PLL, and calculates the RoCoF with the reasonable measurement window of 10 ms.

As seen from Fig. 9, asynchronous Grid A and Grid B are interconnected by a 3000 MVA-rated VSC-HVdc transmission system. Grid A comprises 2 × 2250 MVA synchronous generators, a fixed load L1 of 1050 MW + 210 MVar, and a switchable load L2 of 105 MW + 21 Mvar (10% of the total load in Grid A); Grid B has 2 × 750 MW synchronous generators, a fixed load L3 of 3000 WW + 600 MVar, and a switchable load L4 of 300 MW + 60 Mvar (10% of the total load in Grid B). To analyze the effect of the IEFF for two asynchronous grids with different sizes, Grid A has larger generation but smaller demand as a power sending end, and Grid B has smaller generation but larger demand as a power receiving end. The flow directions of active power are indicated in Fig. 9. The HVdc networks

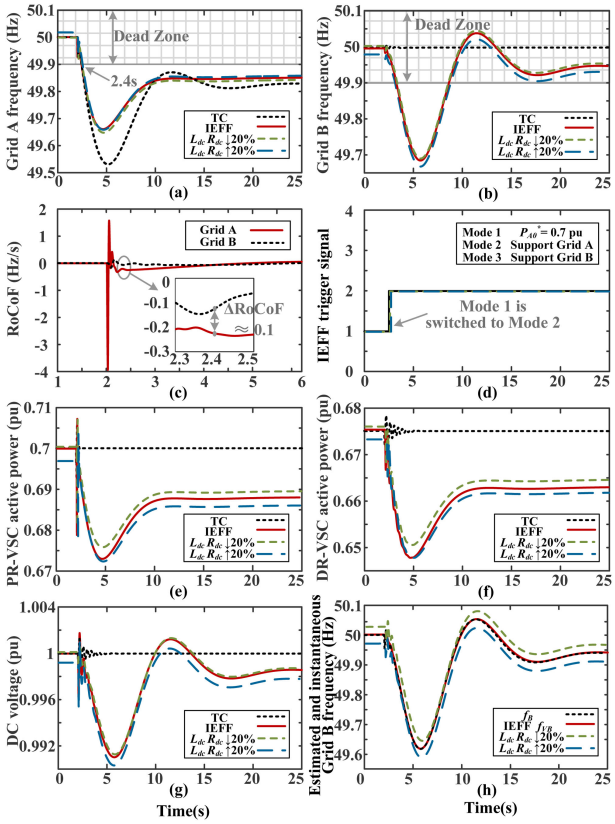

Fig. 10. Comparison of the IEFF and traditional control responses for a 10% load increase in Grid A. (a) Grid A frequency. (b) Grid B frequency. (c) Grid RoCoF. (d) IEFF trigger signal. (e) PR-VSC active power. (f) DR-VSC active power. (g) DC voltage. (h) Estimated f_B.

are modeled in detail as distributed frequency-dependent cables with parameters presented in Table I of Appendix B, in order to verify the accuracy of the frequency information extraction loop. Note that the system frequencies can be settled to a steady state by the standard turbine speed governors as employed in [33] which linearly vary the SG active power outputs with respect to the grid frequencies (primary frequency responses) in the model. As the secondary and/or tertiary frequency modeling analysis is out of focus in this article, the system frequencies may not be returned to the nominal value (50 Hz in this case) under relatively large contingencies.

Three cases are conducted to verify the effectiveness of the IEFF strategy under the selected IEFF parameters of $k_{dc} = 1$, $H = 2$ s, and $D = 5$.

1) Case 1: compare the IEFF performances for PR-VSC under a load increase in Grid A.
2) Case 2: compare the IEFF performances for DR-VSC under a load decline in Grid B.
3) Case 3: compare the IEFF performances under simultaneous ac faults occurring in Grid A and Grid B.

Case 1: Step Load Increase in Grid A

Fig. 10 compares the performances of the proposed IEFF with the aligned circuit and control impedances (red solid curve), the IEFF with R_{dc} and L_{dc} values 20% lower than the values in the control (green dashed curve), the IEFF with R_{dc} and L_{dc}

values 20% higher than the values in the control (blue dashed curve), and the traditional control without IEFF [11] (black dotted curve), under L_2 change at busbar B1 in Grid A at $t = 2$ s.

As can be seen from the Fig. 10(a), with the traditional control, the Grid A frequency decreases from 50 Hz to 49.53 Hz at $t = 5$ s. Immediately when it exceeds the lower threshold of the dead zone (49.9 Hz) approximately at $t = 2.4$ s, the comparison of RoCoFs for Grid A and Grid B is executed in the priority selection control loop in the PR-VSC control. As shown in Fig. 10(c), the Grid A RoCoF is 0.1 Hz / s larger than that of Grid B. Note that the ΔRoCoF is represented as the difference between the absolute values of the RoCoFs of Grid A and Grid B. The priority selection control loop dictates the PR-VSC from Mode 1 (fixed active power control) to Mode 2 (the Grid A supported IEFF), as seen in Fig. 10(d). With the IEFF control, the Grid A frequency drop is significantly reduced by the inertial and droop effects of PR-VSC, which changes the PR-VSC active power and in turn the DR-VSC active power from 0.676 p.u. to 0.663 p.u., see Fig. 10(e) and (f). The DR-VSC active power reduction initiates the Grid B frequency in Fig. 10(b) to drop as well due to the IEFF synchronization mechanism. Consequently, the dc voltage also sees a minor drop, as observed in Fig. 10(g), which is dictated by the V_{dc} / f droop control loop of (3) in the DR-VSC IEFF control. Fig. 10(h) shows the alignment of the Grid B actual frequency and estimated frequency by (4), proving the accuracy of the frequency information extraction loop.

Even with the ±20% dc impedance deviations, the extracted Grid B frequency information in the PR-VSC control by (4) is only slightly discrepant from the actual value (around ±0.025 Hz), as observed in Fig. 10(h). Compared with the IEFF performance under the accurate circuit impedances, this discrepancy causes minor differences in the PR-VSC active power by (5) as seen in Fig. 10(e), and a negligible time delay of mode transition by (7) as seen in Fig. 10(d), and does not affect the IEFF's frequency underpinning performance as shown in Fig. 10(a) and (b).

Case 2: Step Load Decrease in Grid B

Fig. 11 compares the performances of the proposed IEFF control schemes with aligned and misaligned circuit and control impedances, and the traditional control, when the load L4 in Grid B is switched out at $t = 2$ s. With the traditional control, the Grid B frequency rises from 50 to 50.74 Hz at about $t = 5$ s, as shown in Fig. 11(b), without any synchronizing power from Grid A, as seen in the PR-VSC and DR-VSC active powers from Fig. 11(e) and (f). As a result, the Grid A frequency keeps constant, as shown in Fig. 11(a). With the IEFF, the priority selection control loop compares the RoCoFs of Grid A and B in Fig. 11(c). When the Grid A frequency runs out of the dead zone, and the RoCoF difference between Grid A and Grid B at the comparison point is −0.2 Hz/s, the IEFF Mode 1 is then switched to Mode 3 for Grid B frequency support. Under Mode 3, according to the instantaneous Grid B frequency as estimated by the information extraction control loop as shown in Fig. 11(h), the active power from PR-VSC to DR-VSC decreases from 0.7 to 0.664 p.u., as shown in Fig. 11(e) and (f). Although this leads to a minor rise in the Grid A frequency from 50 to 50.14 Hz as

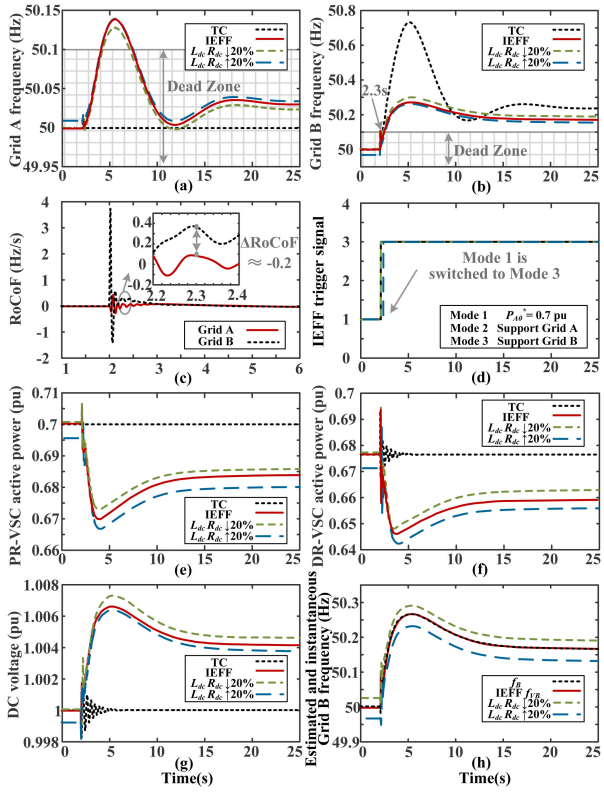

Fig. 11. Comparison of the IEFF and traditional control responses for a 10% load decrease in Grid B. (a) Grid A frequency. (b) Grid B frequency. (c) Grid RoCoF. (d) IEFF selected mode. (e) PR-VSC active power. (f) DR-VSC active power. (g) DC voltage. (h) Estimated f_B.

seen in Fig. 11(a), the IEFF significantly slows down the Grid B RoCoF and also reduces the frequency deviation from 50.74 Hz to 50.28 Hz. The dc voltage is dictated by the V_{dc}/f droop control loop to negligibly increase from 1 to 1.007 p.u. for reflecting the Grid B frequency to the information extraction control loop, as shown in Fig. 11(g). Again, as seen in Fig. 11(h), the estimated frequency f_{VB} is accurately aligned with the actual frequency f_B.

It can be seen in $Case$ 1 and $Case$ 2 that the IEFF emulated inertia can tradeoff the frequency responses of the two interconnected grids. Therefore, the operation conditions and actual inertia levels of both grids must be taken into consideration when setting the emulated inertia and droop for both PR-VSC and DR-VSC. A grid in small size should be set with a larger H and D so as to get more synchronization support, whereas a grid in large size may be set with a small H and D which does not exert apparent impact on the grid stability improvement.

The misalignment of the circuit and control impedances in the circuit and IEFF control loop (as high as ±20%) leads to minor inaccuracy in the Grid B frequency extraction as observed in Fig. 11(h), a negligible time delay of the mode transition as observed in Fig. 11(d), and a small PR-VSC active power deviation as observed in Fig. (e). However, the IEFF with such a misalignment can generally guarantee the control stability and enhance both of the frequency stability in Grid A and Grid B, therefore the general contribution of the IEFF to

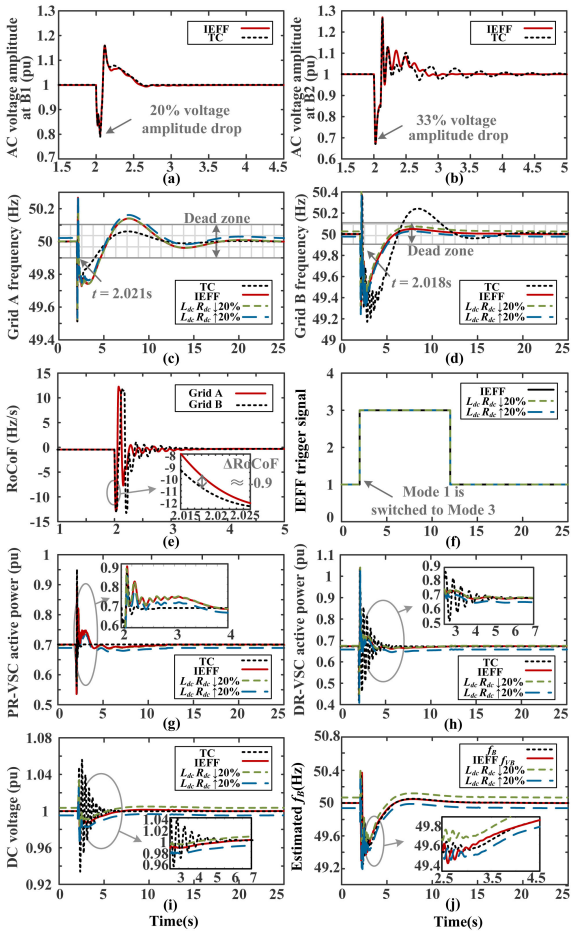

Fig. 12. Comparison of the IEFF and traditional control responses for a 50-ms three-phase-to-ground fault at B1 and 100-ms three-phase-to-ground fault at B2. (a) AC voltage amplitude at B1. (b) AC voltage amplitude at B2. (c) Grid A frequency. (d) Grid B frequency. (e) Grid RoCoF. (f) IEFF selected mode. (g) PR-VSC active power. (h) DR-VSC active power. (i) DC voltage. (j) Estimated f_B.

the asynchronous grids is not affected. On the other hand, as introduced in Section II-B, the periodically calibration of the dc circuit impedance can be carried out to mitigate the impact of such a misalignment on the control accuracy.

Case 3: Large-Signal Disturbances of Simultaneous AC faults in Both Grid A and Grid B

Two temporary 50 ms and 100 ms three-phase-ground ac faults as large-signal disturbances are applied at busbar B1 in Grid A and B2 in Grid B simultaneously at $t = 2$ s as shown in Fig. 12(a) and (b), which results in 20% and 33% voltage dips, respectively. The faults first drive the Grid A and Grid B frequencies [as shown in Fig. 12(c) and (d)] to drop out of the dead zone approximately at $t = 2.02$ s. The Grid B RoCoF is 0.9 Hz/s higher than that of the Grid A as observed in Fig. 12(e), which activates the IEFF Mode 3 to support Grid B as shown in Fig. 12(f). Fig. 12(g) and (h) presents the active power outputs of PR-VSC and DR-VSC, which demonstrates that the PR-VSC active power is varied by the IEFF for DR-VSC inertia and droop emulation. It is worth noticing that the low-frequency oscillations of the DR-VSC active power under the traditional control is also reduced by the IEFF as shown in Fig. 12(h). The oscillation magnitude and recovery time of the Grid B frequency are significantly reduced as seen in Fig. 12(d), by sacrificing a trivial variation in the Grid A frequency as shown in Fig. 12(c). As observed from Fig. 12(i), the dc voltage under the IEFF is controlled to vary, in order to reflect the Grid B frequency information. As shown in Fig. 12(j), despite of small transient deviations, the Grid B frequency as estimated by (4) can satisfactorily track the actual Grid B frequency. As soon as the frequencies of Grid A and Grid B returns to the dead zones after the fault is cleared and the minimum service duration of 10 s is completed, Mode 3 is switched back to Mode 1 as seen in Fig. 12(f) at $t = 12$ s. It can be clearly concluded from this case study that the IEFF opts to support the grid with severer fault conditions and significantly damps out the frequency oscillation, improving the system fault ride-through capability.

Again, the relatively high discrepancy ($\pm 20\%$) in the dc impedance and control impedances leads to the minor differences in the extracted Grid B frequency information and the PR-VSC active power. The overall frequency stability underpinning performance of the IEFF is unaffected and secured as seen from Fig. 12.

V. Conclusion

This article proposes an IEFF strategy for a point-to-point VSC-HVdc transmission system, to enable the converters with mutual frequency support capability. With the proposed IEFF scheme, the inertial and frequency-droop responses for both converter terminals of the VSC-HVdc system can be provided without the need of communications and autonomously prioritize the support to the grid with lower frequency stability. This is achieved by the following four control units: 1) the dc voltage / frequency droop control loop in the dc voltage regulating VSC (DR-VSC); 2) the frequency information extraction loop; 3) the active power regulating VSC (PR-VSC) active power reference modification control loop; 4) a priority selection control loop which compares the severity of the disturbances in both interconnected grids and determines the supported grid in the PR-VSC control. From the controller hardware-in-the-loop experiments, it can be concluded that the IEFF can promote the power synchronization of the interconnected ac grids in forms of the inertial and frequency-droop responses, underpin the frequency stability of both grids by reducing frequency change rate as well as frequency deviation, and suppress angular oscillations under fault conditions. It is anticipated that, with higher degree of asynchronous grid interconnections and further reduced system inertia and damping effects in the future, the IEFF can play an important role in safeguarding the stable and reliable operations of the power grids. It should be noted that although this article only focuses on the point-to-point VSC-HVdc transmission systems, the IEFF can be easily extended to a multiterminal VSC-HVdc system with the same mutual frequency support effect.

APPENDIX

A. State-Space Modeling

The basic topology of the two-area power grid connected by VSC-HVdc is shown in Fig. 5, including ac networks of Grid A and Grid B, dc transmission lines, VSC-HVdc converters and its control system.

1) Synchronous Generator State-Space Model: The adopted SG model considers the electrical characteristics of the stator, excitation, and damper windings. Take one SG generator as an example, the input variable $\Delta\mathbf{u} = [\Delta \boldsymbol{I}_{sg6\times1}, \Delta \boldsymbol{V}_{sg6\times1}, \Delta T_m, \Delta T_e]$, and the state variable $\Delta\mathbf{x} = [\Delta\boldsymbol{\varphi}_{sg6\times1}, \Delta\omega_r, \Delta\theta_{sg}]$. Then the state matrix $\boldsymbol{A}_{sg}$ and input matrix $\boldsymbol{B}_{sg}$ are

$$\boldsymbol{A}_{sg} = \begin{bmatrix} -\boldsymbol{\omega}_{6\times6} & \boldsymbol{\varphi}_{6\times1} & 0 \\ 0 & -\dfrac{D}{2H} & 0 \\ 0 & 1 & 0 \end{bmatrix}$$

$$\boldsymbol{B}_{sg} = \begin{bmatrix} -\boldsymbol{R}_{6\times6} & 1 & 0 & 0 \\ 0 & 0 & \dfrac{1}{2H} & -\dfrac{1}{2H} \\ 0 & 0 & 0 & 0 \end{bmatrix}$$

T_m and T_e is calculated by the following:

$$\begin{cases} \Delta T_m = \dfrac{\Delta P_M}{\Delta\omega_r} \\ \Delta T_e = \Delta\varphi_d i_q + \varphi_d \Delta i_q - \Delta\varphi_q i_d - \varphi_q \Delta i_d. \end{cases} \tag{10}$$

2) Steam Turbine Governor and Excitation System State-Space Model: The modeling in this article uses a fourth-order steam turbine [34], [35]. For the turbine governor and excitation system, the input variables $\Delta\mathbf{u} = [\Delta v_m, \Delta v_f, \Delta\omega_r, \Delta g]$, and the state variables $\Delta\mathbf{x} = [\Delta v_{mf}, \Delta v_{fd}, \Delta v_f, \Delta g, \Delta g_1, \Delta T_{t2}, \Delta T_{t3}, \Delta T_{t4}, \Delta T_{t5}]$. The state matrix $\boldsymbol{A}_{stg}$ and input matrix $\boldsymbol{B}_{stg}$ are

$$\boldsymbol{A}_{stg} = \begin{bmatrix} -\dfrac{1}{T_r} & 0 & 0 & & & & & \\ 0 & -\dfrac{1}{T_{fd}} & 0 & \boldsymbol{0}_{3\times2} & & \boldsymbol{0}_{3\times4} & & \\ -\dfrac{K_a}{T_a} & -\dfrac{K_a}{T_a} & -\dfrac{1}{T_a} & & & & & \\ & & & -\dfrac{1}{T_{sm}} & \dfrac{1}{T_{sm}} & & & \\ & \boldsymbol{0}_{2\times3} & & 0 & -\dfrac{1}{T_{sr}} & \boldsymbol{0}_{2\times4} & & \\ & & & & & -\dfrac{1}{T_1} & \dfrac{1}{T_1} & 0 & 0 \\ & & & & & 0 & -\dfrac{1}{T_2} & \dfrac{1}{T_2} & 0 \\ & \boldsymbol{0}_{4\times3} & & \boldsymbol{0}_{4\times2} & & 0 & 0 & -\dfrac{1}{T_3} & \dfrac{1}{T_3} \\ & & & & & 0 & 0 & 0 & -\dfrac{1}{T_4} \end{bmatrix}$$

$$\boldsymbol{B}_{stg} = \begin{bmatrix} \dfrac{1}{T_r} & 0 & & \\ 0 & \dfrac{K_{fd}}{T_{fd}} & \boldsymbol{0}_{3\times1} & \boldsymbol{0}_{3\times1} \\ 0 & 0 & & \\ & & 0 & \\ \boldsymbol{0}_{2\times2} & & -\dfrac{K_pR_p}{T_{sr}} & \boldsymbol{0}_{2\times1} \\ & & & 0 \\ & & & 0 \\ \boldsymbol{0}_{4\times2} & & \boldsymbol{0}_{4\times1} & 0 \\ & & & \dfrac{1}{T_4} \end{bmatrix}.$$

Among them, v_m is calculated by the dq-axis voltage vectors of the synchronous generator as

$$\Delta v_m = \sqrt{v_{sgd}^2 + 2v_{sgd}\Delta v_{sgd} + v_{sgq}^2 + 2v_{sgq}\Delta v_{sgq}}. \tag{11}$$

Through the governor control, the mechanical power input to the synchronous generator can be calculated as

$$\begin{cases} \Delta T_{t1} = F_2\Delta T_{t2} + F_3\Delta T_{t3} + F_4\Delta T_{t4} + F_5\Delta T_{t5} \\ \Delta P_M = \Delta T_{t1}\omega_r + T_{t1}\Delta\omega_r. \end{cases} \tag{12}$$

3) SG Transformer and RC Load State-Space Model: For the SG transformer, the input variables $\Delta\mathbf{u} = [\Delta v_{sgd} - \Delta v_{sd}, \Delta v_{sgq} - \Delta v_{sq}, \Delta i_{cd}, \Delta i_{cq}]$, and the state variables $\Delta\mathbf{x} = [\Delta i_{td}, \Delta i_{tq}, \Delta v_{cd}, \Delta v_{cq}]$. Then the state matrix $\boldsymbol{A}_{trc}$ and input matrix $\boldsymbol{B}_{trc}$ are

$$\boldsymbol{A}_{trc} = \begin{bmatrix} -\dfrac{R_t}{L_t} & \omega_{pll} & & \\ -\omega_{pll} & -\dfrac{R_t}{L_t} & \boldsymbol{0}_{2\times2} & \\ & & 0 & \omega_{pll} \\ \boldsymbol{0}_{2\times2} & & -\omega_{pll} & 0 \end{bmatrix}$$

$$\boldsymbol{B}_{trc} = \begin{bmatrix} 1 & 0 & & \\ 0 & 1 & \boldsymbol{0}_{2\times2} & \\ & & \dfrac{1}{C_{rc}} & \omega_{pll}R_{rc} \\ \boldsymbol{0}_{2\times2} & & -\omega_{pll}R_{rc} & \dfrac{1}{C_{rc}} \end{bmatrix}.$$

The terminal voltage of the *RC* load can be expressed as

$$\begin{cases} \Delta v_{sd} = \Delta v_{cd} + \Delta i_{cd}R_{rc} \\ \Delta v_{sq} = \Delta v_{cq} + \Delta i_{cq}R_{rc}. \end{cases} \tag{13}$$

4) Converter Control System State-Space Model: For PR-VSC, the input variables $\Delta\mathbf{u} = [\Delta u_{s1d} - \Delta u_{r1d}, \Delta u_{s1q} - \Delta u_{r1q}]$, and the state variables $\Delta\mathbf{x} = [\Delta i_{s1d}, \Delta i_{s1q}]$; for DR-VSC, the input variables $\Delta\mathbf{u} = [\Delta u_{s2d} - \Delta u_{r2d}, \Delta u_{s2q} -$

$\Delta u_{r2q}]$, and the state variables $\Delta \mathbf{x} = [\Delta i_{s2d}, \Delta i_{s2q}]$. Then, the state matrix $\boldsymbol{A}_c$ and input matrix $\boldsymbol{B}_c$ are

$$\boldsymbol{A}_c = \begin{bmatrix} -\dfrac{R_c}{L_c} & \omega_{pll} \\ -\omega_{pll} & -\dfrac{R_c}{L_c} \end{bmatrix} \boldsymbol{B}_c = \begin{bmatrix} 1 & 0 \\ 0 & 1 \end{bmatrix}.$$

The small-signal equations for the PR-VSC outer loops are

$$\begin{cases} \Delta i_d^* = \left(k_{pp} + \dfrac{k_{ip}}{s}\right)\left({P_A}^* - \Delta P_A\right) \\ \Delta i_q^* = \left(k_{pq1} + \dfrac{k_{iq1}}{s}\right)\left(\Delta Q_A - {Q_A}^*\right) \end{cases} \tag{14}$$

$$\begin{cases} \Delta i_d^* = k_{pp}{P_A}^* - k_{pp}\Delta P_A + \Delta z_{1i} \\ \Delta i_q^* = k_{pq1}{Q_A}^* - k_{pq1}\Delta Q_A + \Delta z_{2i}. \end{cases} \tag{15}$$

The small-signal equations for the DR-VSC outer loops are

$$\begin{cases} \Delta i_d^* = \left(k_{pdc} + \dfrac{k_{idc}}{s}\right)\left({V_{dcB}}^* - \Delta V_{dcB}\right) \\ \Delta i_q^* = \left(k_{pq2} + \dfrac{k_{iq2}}{s}\right)\left(\Delta Q_B - {Q_B}^*\right) \end{cases} \tag{16}$$

$$\begin{cases} \Delta i_d^* = k_{pdc}{V_{dcB}}^* - k_{pdc}\Delta V_{dcB} + \Delta z_{3i} \\ \Delta i_q^* = k_{pq2}{Q_B}^* - k_{pq2}\Delta Q_B + \Delta z_{4i}. \end{cases} \tag{17}$$

The small-signal equations for the inner current loops are

$$\begin{cases} \Delta v_d^* = \Delta v_{sd} + \omega_{pll}L_c\Delta i_q - \left(k_{pi} + \dfrac{k_{ii}}{s}\right)\left(i_d^* - \Delta i_{sd}\right) \\ \Delta v_q^* = \Delta v_{sq} - \omega_{pll}L_c\Delta i_d - \left(k_{pi} + \dfrac{k_{ii}}{s}\right)\left(i_q^* - \Delta i_{sq}\right) \end{cases} \tag{18}$$

$$\begin{cases} \Delta v_d^* = \Delta v_{sd} + \omega_{pll}L_c\Delta i_q - k_{pi}(\Delta i_d^* - \Delta i_{sd}) - \Delta z_{5i} \\ \Delta v_q^* = \Delta v_{sq} - \omega_{pll}L_c\Delta i_d - k_{pi}(\Delta i_q^* - \Delta i_{sq}) - \Delta z_{6i}. \end{cases} \tag{19}$$

The small-signal equations for the PLLs are

$$\begin{cases} \Delta\theta = \dfrac{1}{s}\Delta\omega_{pll} \\ \Delta\omega_{pll} = \left(k_p + \dfrac{k_i}{s}\right)\Delta v_{sq}. \end{cases} \tag{20}$$

5) DC System State-Space Model: For the dc transmission system, the input variables $\Delta \mathbf{u} = [\Delta i_{dcA}, \Delta i_{dcB}]$, and the state variables $\Delta \mathbf{x} = [\Delta V_{dcA}, \Delta V_{dcB}, \Delta I_{dc}]$. Then the state matrix $\boldsymbol{A}_{dc}$ and input matrix $\boldsymbol{B}_{dc}$ are

$$\boldsymbol{A}_{dc} = \begin{bmatrix} 0 & 0 & -\dfrac{1}{C} \\ 0 & 0 & \dfrac{1}{C} \\ \dfrac{1}{L_{dc}} & -\dfrac{1}{L_{dc}} & -\dfrac{R_{dc}}{L_{dc}} \end{bmatrix}$$

$$\boldsymbol{B}_{dc} = \frac{1}{C}\begin{bmatrix} 1 & 0 \\ 0 & -1 \\ 0 & 0 \end{bmatrix}.$$

Based on the dc power equation, the current of the dc system can be described as

$$\begin{cases} \Delta i_{dcA} = \dfrac{\Delta P_{PR-VSC}}{\Delta V_{dcA}} \\ \Delta i_{dcB} = \dfrac{\Delta P_{DR-VSC}}{\Delta V_{dcB}}. \end{cases} \tag{21}$$

B. Parameters for the VSC-HVDC System and the Two-Area System

TABLE I
PARAMETERS OF THE VSC-HVDC LINK

Item	Value
Rated VSC power S_{vsc}	3 GVA
DC capacitor C_{dc}	100 μF
Nominal DC voltage V_{dcB0}	1900 kV
Rated VSC AC rms voltage V_{vsc}	1100 kV
System frequency	50 Hz
Reactor inductance L	0.3 pu
Reactor resistance R	0.03 pu
DC cable resistance r	9 m$\Omega \cdot$ m^{-1}
DC cable inductance l	0.33 mH $\cdot$ m^{-1}
DC cable capacitance c	0.31 μF $\cdot$ m^{-1}

TABLE II
PARAMETERS OF SYNCHRONOUS GENERATOR

Item	Value
Rated SS GW S_g	4.5 GW
Rated RS GW S_g	1.5 GW
Terminal Voltage V_g	20 kV
SS inertia time constant	6.5 s
RS inertia time constant	6.175 s
$x_d, x_d^{'}, x_d^{''}$	1.8, 0.3, 0.25
$x_q, x_q^{''}, x_1$	1.7, 0.55, 0.2
$t_d^{'}, t_d^{''}, t_q^{'}, t_q^{''}$	8, 0.03, 0.4, 0.5 s
Stator resistance R_s	0.0025
Turbine permanent droop R_P	0.05
Exciter regulator gain	200
Exciter time constant	0.001 s

TABLE III
PARAMETERS OF VSC CONTROLLERS

Station	Parameter	Value
PR-VSC	Outer controller loop (k_{pp},k_{ip})	(0.5,20)
	Inner controller loop (k_{p1},k_{i1})	(0.15,15)
	PLL (k_{p2},k_{i2})	(60,1400)
DR-VSC	Outer controller loop (k_{pdc},k_{idc})	(2,50)
	Inner controller loop (k_{p3},k_{i3})	(0.8,350)
	PLL (k_{p4},k_{i4})	(60,1400)

TABLE IV
EIGENVALUES OF TESTED SSM SYSTEM

λ	Eigenvalue	Damping ratio	f(Hz)
λ_1 & λ_2	-585355.36±310.52i	1	49.42
λ_3 & λ_4	-128905.63±318.81i	0.99	50.74
λ_5	-3497.18	1	0
λ_6	-3763.43	1	0
λ_7	-3828.91	1	0
λ_8	-2214.89	1	0
λ_9	-1001.34	1	0
λ_{10}	-998.14	1	0
λ_{11}	-999.99	1	0
λ_{12}	-999.99	1	0
λ_{13}	-551.40	1	0
λ_{14} & λ_{15}	-440.65±379.07i	0.758	60.33
λ_{16} & λ_{17}	-223.75±425.19i	0.466	67.67
λ_{18} & λ_{19}	-135.50±96.92i	0.813	15.43
λ_{20} & λ_{21}	-118.68±92.85i	0.788	14.78
λ_{22}	-49.29	1	0
λ_{23}	-49.10	1	0
λ_{24} & λ_{25}	-30.76±17.98i	0.863	2.86
λ_{26} & λ_{27}	-29.62±18.42i	0.849	2.93
λ_{28}	-33.63	1	0
λ_{29}	-20.94	1	0
λ_{30}	-20.81	1	0
λ_{31} & λ_{32}	-16.26±23.36i	0.571	3.72
λ_{33} & λ_{34}	-14.53±21.60i	0.558	3.44
λ_{35} & λ_{36}	-13.51±0.40i	0.999	0.06
λ_{37} & λ_{38}	-7.54±321.76i	0.023	51.21
λ_{39}	-6.83	1	0
λ_{40}	-6.84	1	0
λ_{41} & λ_{42}	-4.83±14.18i	0.322	2.26
λ_{43}	-4.45	1	0
λ_{44}	-2.75	1	0
λ_{45} & λ_{46}	-2.51±314.41i	0.008	50.04
λ_{47}	-1.48	1	0
λ_{48}	-1.33	1	0
λ_{49} & λ_{50}	-0.67±314.41i	0.002	50.04
λ_{51} & λ_{52}	-0.49±0.48i	0.714	0.08
λ_{53} & λ_{54}	-0.28±321.76i	0.001	51.21
λ_{55} & λ_{56}	-0.28±0.50i	0.489	0.08
λ_{57}	-0.18	1	0
λ_{58}	-0.17	1	0

REFERENCES

[1] "BP statistical review of world energy," bp p.l.c., London, U.K., 2020. [Online]. Available: https://www.bp.com/content/dam/bp/business-sites/en/global/corporate/pdfs/energy-economics/statistical-review/bp-stats-review-2020-full-report.pdf

[2] "Ten year network development plan," ENTSOG, Brussels, Belgium, 2020. [Online]. Available: https://www.entsog.eu/

[3] J. Fan, X. Wang, Q. Huang, X. Zhang, Y. Li, and P. Zeng, "Power grid interconnection with HVDC link in Northeast Asia considering complementarity of renewable energy and time zone difference," *J. Eng.*, vol. 2019, no. 16, pp. 1625–1629, 2019.

[4] Z. Liu, G. Chen, X. Guan, Q. Wang, and W. He, "A concept discussion on Northeast Asia power grid interconnection," *CSEE J. Power Energy Syst.*, vol. 2, no. 4, pp. 87–93, 2016.

[5] N. Flourentzou, V. G. Agelidis, and G. D. Demetriades, "VSC-based HVDC power transmission systems: An overview," *IEEE Trans. Power Electron.*, vol. 24, no. 3, pp. 592–602, Mar. 2009.

[6] D. Xu, X. Zhao, Y. Lu, K. Qin, and L. Guo, "Study on overvoltage of hybrid LCC-VSC-HVDC transmission," *J. Eng.*, vol. 2019, no. 16, pp. 1906–1910, 2019.

[7] J. Zhu *et al.*, "Coordinated flexible damping mechanism with inertia emulation capability for MMC-MTDC transmission systems," *IEEE J. Emerg. Sel. Topics Power Electron.*, vol. 9, no. 6, pp. 7329–7342, Dec. 2021.

[8] Q. C. Zhong, "Virtual synchronous machines: A unified interface for grid integration," *IEEE Power Electron. Mag.*, vol. 3, no. 4, pp. 18–27, Dec. 2016.

[9] Q. C. Zhong and G. Weiss, "Synchronverters: Inverters that mimic synchronous generators," *IEEE Trans. Ind. Electron.*, vol. 58, no. 4, pp. 1259–1267, Apr. 2011.

[10] L. Zhang, L. Harnefors, and H. P. Nee, "Power-synchronization control of grid-connected voltage-source converters," *IEEE Trans. Power Syst.*, vol. 25, no. 2, pp. 809–820, May 2010.

[11] E. Rakhshani, D. Remon, A. M. Cantarellas, J. M. Garcia, and P. Rodriguez, "Virtual synchronous power strategy for multiple HVDC interconnections of multi-area AGC power systems," *IEEE Trans. Power Syst.*, vol. 32, no. 3, pp. 1665–1677, May 2017.

[12] C. Guo, W. Liu, C. Zhao, and R. Iravani, "A frequency-based synchronization approach for the VSC-HVDC station connected to a weak AC grid," *IEEE Trans. Power Del.*, vol. 32, no. 3, pp. 1460–1470, Jun. 2017.

[13] D. Pan, X. Wang, F. Liu, and R. Shi, "Transient stability of voltage-source converters with grid-forming control: A design-oriented study," *IEEE Trans. Emerg. Sel. Topics Power Electron.*, vol. 8, no. 2, pp. 1019–1033, Jun. 2020.

[14] J. Zhu, C. D. Booth, G. P. Adam, A. J. Roscoe, and C. G. Bright, "Inertia emulation control strategy for VSC-HVDC transmission systems," *IEEE Trans. Power Syst.*, vol. 28, no. 2, pp. 1277–1287, May 2013.

[15] J. Zhu *et al.*, "Synthetic inertia control strategy for doubly fed induction generator wind turbine generators using lithium-ion supercapacitors," *IEEE Trans. Energy Convers.*, vol. 33, no. 2, pp. 773–783, Jun. 2018.

[16] Z. Shen *et al.*, "Variable-inertia emulation control scheme for VSC-HVDC transmission systems," *IEEE Trans. Power Syst.*, vol. 37, no. 1, pp. 629–639, Jan. 2022.

[17] Y. Li, Z. Zhang, Y. Yang, Y. Li, H. Chen, and Z. Xu, "Coordinated control of wind farm and VSC-HVDC system using capacitor energy and kinetic energy to improve inertia level of power systems," *Int. J. Elect. Power Energy Syst.*, vol. 59, pp. 79–92, 2014.

[18] F. Nejabatkhah and Y. W. Li, "Overview of power management strategies of hybrid AC/DC microgrid," *IEEE Trans. Power Electron.*, vol. 30, no. 12, pp. 7072–7089, Dec. 2015.

[19] M. Andreasson, D. V. Dimarogonas, H. Sandberg, and K. H. Johansson, "Distributed controllers for multiterminal HVDC transmission systems," *IEEE Trans. Control Netw. Syst.*, vol. 4, no. 3, pp. 564–574, Sep. 2017.

[20] A. Kirakosyan, E. F. El-Saadany, M. S. El Moursi, and K. Al Hosani, "DC voltage regulation and frequency support in pilot voltage droop-controlled multiterminal HVDC systems," *IEEE Trans. Power Del.*, vol. 33, no. 3, pp. 1153–1164, Jun. 2018.

[21] Z. Li, Z. Wei, R. Zhan, Y. Li, Y. Tang, and X.-P. Zhang, "Frequency support control method for interconnected power systems using VSC-MTDC," *IEEE Trans. Power Syst.*, vol. 36, no. 3, pp. 2304–2313, May 2021.

[22] M. Gao, M. Chen, C. Wang, and Z. Qian, "An accurate power-sharing control method based on circulating-current power phasor model in voltage-source inverter parallel-operation system," *IEEE Trans. Power Electron.*, vol. 33, no. 5, pp. 4458–4476, May 2018.

[23] J. M. Guerrero, J. C. Vasquez, J. Matas, L. G. De Vicuña, and M. Castilla, "Hierarchical control of droop-controlled AC and DC microgrids–A general approach toward standardization," *IEEE Trans. Ind. Electron.*, vol. 58, no. 1, pp. 158–172, Jan. 2011.

[24] M. A. Abdelwahed and E. F. El-Saadany, "Power sharing control strategy of multiterminal VSC-HVDC transmission systems utilizing adaptive voltage droop," *IEEE Trans. Sustain. Energy*, vol. 8, no. 2, pp. 605–615, Apr. 2017.

[25] Y. Phulpin, "Communication-free inertia and frequency control for wind generators connected by an HVDC-link," *IEEE Trans. Power Syst.*, vol. 27, no. 2, pp. 1136–1137, May 2012.
[26] B. Silva, C. Moreira, L. Seca, Y. Phulpin, and J. A. Pecas Lopes, "Provision of inertial and primary frequency control services using offshore multiterminal HVDC networks," *IEEE Trans. Sustain. Energy*, vol. 3, no. 4, pp. 800–808, Oct. 2012.
[27] O. D. Adeuyi, M. Cheah-Mane, J. Liang, and N. Jenkins, "Fast frequency response from offshore multiterminal VSC-HVDC schemes," *IEEE Trans. Power Del.*, vol. 32, no. 6, pp. 2442–2452, Dec. 2017.
[28] H. Liu and Z. Chen, "Contribution of VSC-HVDC to frequency regulation of power systems with offshore wind generation," *IEEE Trans. Energy Convers.*, vol. 30, no. 3, pp. 918–926, Sep. 2015.
[29] A. Rodríguez-Cabero, J. Roldán-Pérez, M. Prodanovic, J. A. Suul, and S. D'Arco, "Virtual friction control for power system oscillation damping with VSC-HVDC links," in *Proc. IEEE Energy Convers. Congr. Expo.*, 2019, pp. 6495–6500.
[30] A. Rodríguez-Cabero, J. Roldán-Pérez, M. Prodanovic, J. A. Suul, and S. D'Arco, "Coupling of AC grids via VSC-HVDC interconnections for oscillation damping based on differential and common power control," *IEEE Trans. Power Electron.*, vol. 35, no. 6, pp. 6548–6558, Jun. 2020.
[31] S. Gustafsson *et al.*, "Electromagnetic dispersion modeling and measurements for HVDC power cables," *IEEE Trans. Power Del.*, vol. 29, no. 6, pp. 2439–2447, Dec. 2014.
[32] Security and quality of supply standard, national grid, London, U.K., 2018. [Online]. Available: https://www.nationalgrideso.com/industry-information/codes/security-and-quality-supply-standards
[33] P. Kundur, N. J. Balu, and M. G. Lauby, *Power System Stability and Control*. New York, NY, USA: McGraw-Hill, 1994.
[34] I. C. Report, "Dynamic models for steam and hydro turbines in power system studies," *IEEE Trans. Power App. Syst.*, vol. PAS-92, no. 6, pp. 1904–1915, Nov. 1973.
[35] R. Farmer, "Second benchmark model for computer simulation of subsynchronous resonance IEEE subsynchronous resonance working group of the dynamic system performance subcommittee power system engineering committee," *IEEE Power Eng. Rev.*, vol. 5, no. 5, pp. 34–34, May 1985.

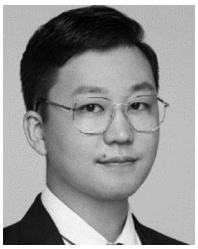

Jiebei Zhu (Senior Member, IEEE) received the Ph.D. degree in electronic and electrical engineering from the University of Strathclyde, Glasgow, U.K., in 2013.

Between 2013 and 2018, he acted as a Senior Power System Engineer and Innovation Project Manager with U.K. National Grid Plc., London, U.K., where he was involved with the modeling, development, and real-time operation of the GB transmission system. Since 2018, he has been a Professor with the School of Electrical and Information Engineering, Tianjin University, Tianjin, China. His research interests include novel control and operation of ac/dc transmission systems and renewable energy systems.

Dr. Zhu is a Fellow and Chartered Engineer of IET and an Outstanding Young Engineer of the IEEE Power and Energy Society, China.

Xiaonan Wang was born in Hebei, China. She received the B.S. degree from Yanshan University, Qinhuangdao, China, in 2018, and the M.S. degree from Tianjin University, Tianjin, China, in 2021, both in electrical engineering.

Her research interests include control of VSC-HVdc and power system frequency stability.

Junbo Zhao (Senior Member, IEEE) received the Ph.D. degree in electrical engineering from the Department of Electrical and Computer Engineering, Virginia Tech, Blacksburg, VA, USA, in 2018.

He is currently with the University of Connecticut, Storrs, CT, USA. His research interests include cyber-physical power system modeling, estimation, security, dynamics, and stability, uncertainty quantification, robust statistical signal processing, and machine learning for smart grid.

Lujie Yu received the B.S. and M.S. degrees from North China Electric Power University, Beijing, China, in 2012 and 2015, respectively, and the Ph.D. degree from the University of Strathclyde, Glasgow, U.K., in 2019.

He is currently a Lecturer with the School of Electrical and Information Engineering, Tianjin University, Tianjin, China. His research interests include HVdc transmision system and wind power integration.

Suxuan Li was born in Tangshan, Hebei, China, in 1997. She received the B.S. degree in electrical engineering from Northeast Agricultural University, Harbin, China, in 2019. She is currently working toward the master's degree in electrical engineering with Tianjin University, Tianjin, China.

Her research interests include hybrid HVdc control strategy and stability analysis.

Yunwei Li (Fellow, IEEE) received the B.Sc. degree in electrical engineering from Tianjin University, Tianjin, China, in 2002, and the Ph.D. degree from Nanyang Technological University, Singapore, in 2006.

He is currently a Professor with the University of Alberta, Edmonton, AB, Canada. His research interests include distributed generation, microgrid, renewable energy, high-power converters, and electric motor drives.

Dr. Li is an Editor-in-Chief for the IEEE TRANSACTIONS ON POWER ELECTRONICS LETTERS. He is listed as a Highly Cited Researcher by the Web of Science Group.

Josep M. Guerrero (Fellow, IEEE) received the B.S. degree in telecommunications engineering, the M.S. degree in electronics engineering, and the Ph.D. degree in power electronics from the Technical University of Catalonia, Barcelona, Spain, in 1997, 2000, and 2003, respectively.

Since 2011, he has been a Full Professor with the Department of Energy Technology, Aalborg University, Aalborg, Denmark, where he is currently responsible for the Microgrid Research Program.

Dr. Guerrero was the recipient of the Clarivate Analytics (former Thomson Reuters) as the Highly Cited Researcher with 50 highly cited papers, for seven consecutive years, from 2014 to 2020. He is also an Associate Editor for a number of IEEE Transactions.

Chengshan Wang (Senior Member, IEEE) received the B.Sc., M.Sc., and Ph.D. degrees from Tianjin University, Tianjin, China, in 1983, 1985, and 1991, respectively.

From 1994 to 1996, he was a Visiting Scientist with Cornell University, Ithaca, NY, USA. He became a Full Professor with Tianjin University in 1996. From 2001 to 2002, he was a Visiting Professor with Carnegie Mellon University, Pittsburgh, PA, USA. He is an Academician with China Engineering Academy, the Chief Scientist of 973 Project "Research on the Key Issues of Distributed Generation Systems." His research interests include distribution system analysis and planning, distributed generation system and microgrid, and power system security analysis. He was the recipient of the National Science Fund for Distinguished Young Scholars.